ACS OMEGA

Article

http://pubs.acs.org/journal/acsodf

Scalable Route to the Fabrication of $CH_3NH_3PbI_3$ Perovskite Thin Films by Electrodeposition and Vapor Conversion

Georgi Popov,* Miika Mattinen, Marianna L. Kemell, Mikko Ritala, and Markku Leskelä

Department of Chemistry, University of Helsinki, P.O. Box 55, A. I. Virtasen aukio 1, FI-00014 Helsinki, Finland

Supporting Information

ABSTRACT: Hybrid halide perovskite thin films are applicable in a wide range of devices such as light-emitting diodes, solar cells, and photodetectors. The optoelectronic properties of perovskites together with their simple and inexpensive film deposition methods make these materials a viable alternative to established materials in these devices. However, the potential of perovskite materials is compromised by the limitations of the existing deposition methods, which suffer from trade-off among suitability for large-scale industrial production in a batch or roll-to-roll manner, deposition area, film quality, and costs. We addressed these limitations by developing a deposition method that is inexpensive, applicable to large substrate areas, scalable, and yields high-quality perovskite films. In this study, the low-cost electrodeposition (ED) method and sequential exposure to reagent vapors produce $CH_3NH_3PbI_3$ perovskite films with thickness nonuniformity below 9% on a centimeter scale. PbO_2 films are electrodeposited first and then undergo two vapor conversion steps, with HI vapor in the first step and CH_3NH_3I vapor in the second step. The second step yields $CH_3NH_3PbI_3$ films that are continuous and consist of micrometer-sized grains. This process allows the preparation of both α- and β-phase $CH_3NH_3PbI_3$ films, offers a simple means to control the film thickness, and works over a wide range of film thicknesses. In this work, films with thicknesses ranging from 100 nm to 10 μm were prepared. ED and vapor conversion are inherently scalable techniques and hence the process described herein could benefit application areas in which large device areas and throughput are required, such as the production of solar cells.

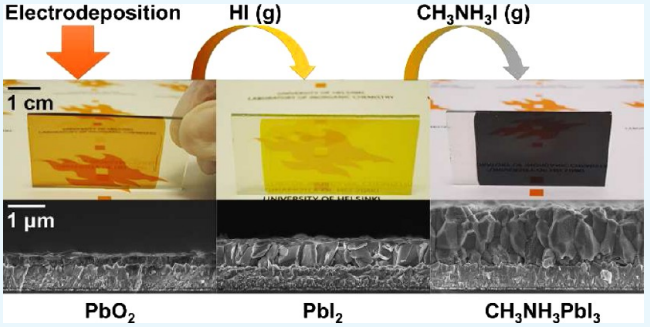

INTRODUCTION

Hybrid halide perovskites (hereafter perovskites), such as $CH_3NH_3PbI_3$ (hereafter $MAPbI_3$), are a recently emerged class of materials that can be employed in light-emitting diodes (LEDs),[1,2] thin-film transistors (TFTs),[3] optically pumped lasers,[4] photodetectors,[5,6] resistive switching random access memory (ReRAM),[7] and solar water splitting;[8] however, they are perhaps the most known for enabling high efficiency in solution-processed photovoltaic devices. Perovskites are commended for their inexpensive processing methods as well as for their optical and electronic properties. These properties, for example, allow perovskite-based solar cells to reach efficiencies comparable to those of other established thin-film solar cell technologies, such as those that employ cadmium telluride or copper indium gallium selenide.[9]

Perovskite devices with different architectures are described in the literature. The photovoltaic architectures are the most diverse ones, with the devices relying on mesoporous scaffolds,[10−12] nanostructures,[13−16] planar thin films,[17−19] and hybrids thereof, whereas other perovskite application areas mostly rely on thin-film architectures.[2−4,7] Of late, in the area of high-efficiency perovskite photovoltaics, the focus has moved to architectures composed of planar thin films.[20,21] For perovskite films, uniformity and low grain boundary density (large grains) are some of the major requirements for improving device performance.[3,7,22,23] The most common approach for depositing perovskites is spin coating.[24] Spin-coating approaches can be further divided into those relying on single-step,[25] two-step,[11] and solvent-engineering[21] methods. All of these methods are capable of producing perovskite films of sufficient quality. However, in spin coating, the film quality deteriorates with increasing deposition area. For that reason, devices prepared using spin-coating-based approaches typically have areas of a couple of square centimeters or less.[2,6,7,26] For example, the most efficient perovskite solar cells commonly have areas of about 0.1 cm^2.[2,27] Devices with larger areas therefore require alternative perovskite deposition methods, which are scalable.

Several scalable deposition methods that do not involve spin coating are applicable for perovskites. These methods rely on physical vapor deposition (PVD),[17,28] chemical vapor deposition (CVD),[29,30] atomic layer deposition (ALD),[31] electrodeposition (ED) combined with conversion in solution,[32] spray deposition (SD),[33,34] and the doctor blade (DB) technique.[35,36]

Received: October 31, 2016
Accepted: December 6, 2016
Published: December 20, 2016

DOI: 10.1021/acsomega.6b00351
ACS Omega 2016, 1, 1296−1306

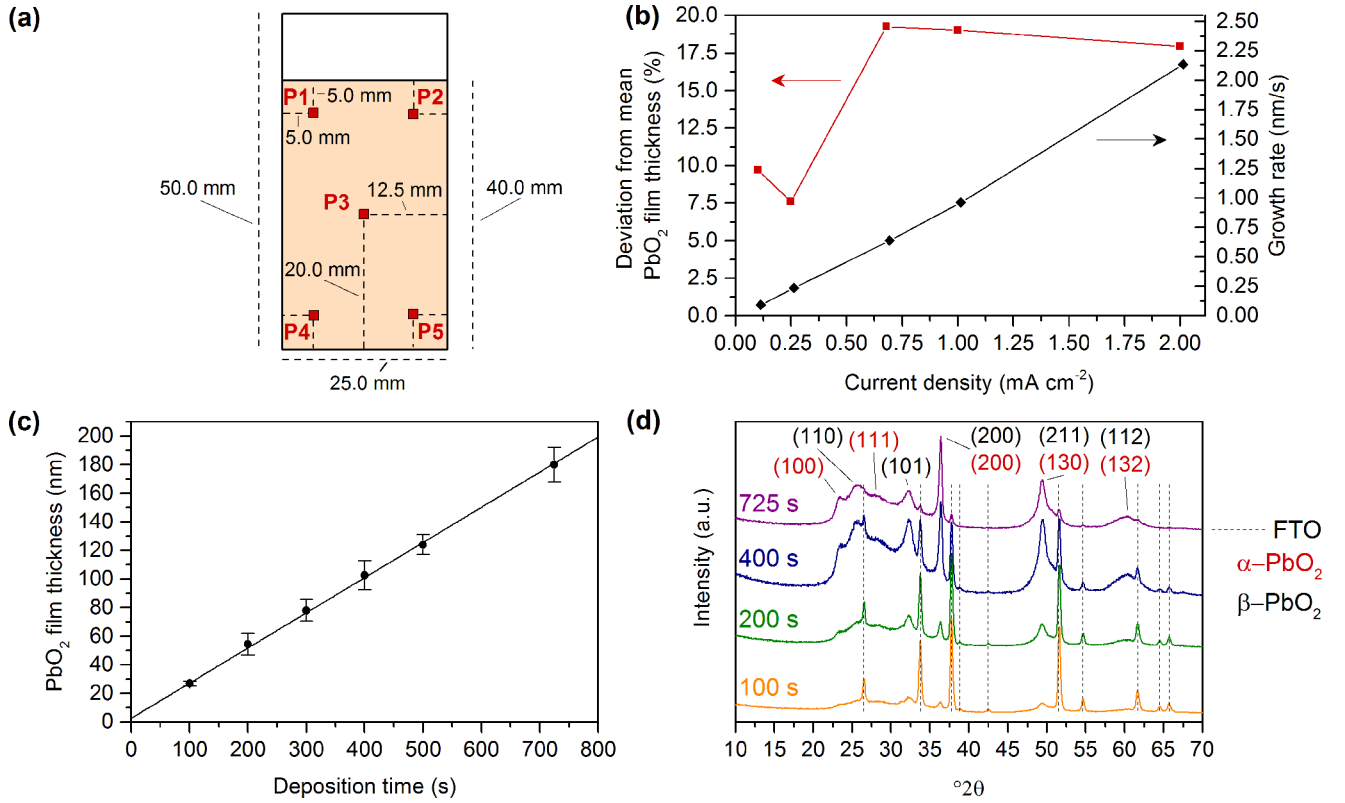

Figure 1. (a) Positions of the thickness measurement points. (b) Standard deviation from the mean PbO_2 film thickness and growth rate as a function of deposition current density. The films were grown for 100 s. (c) PbO_2 thickness as a function of deposition time at a constant current density of 0.25 mA cm^{-2}. Fitted curve R^2 = 0.999. (d) Grazing incidence X-ray diffractograms of PbO_2 films deposited for different times.

Methods employing solutions, such as ED, SD, and DB, yield less-uniform films with a higher grain boundary density, whereas uniform perovskite films, typically with a low grain boundary density, are produced by vacuum techniques, such as PVD, CVD, and ALD. Because vacuum techniques are more expensive than solution-based methods, the existing scalable approaches for perovskite film deposition offer trade-offs between quality and cost.

Herein, we attempted to preserve the advantages of both quality and low-cost by first converting electrodeposited PbO_2 films into PbI_2 films with HI vapor and subsequently converting PbI_2 films into $MAPbI_3$ films with CH_3NH_3I vapor. We further explore the features of this deposition approach and film properties, such as thickness controllability and uniformity, that are important in a variety of perovskite film application areas. ED is a simple and inexpensive method that is applicable for the deposition of uniform coatings on substrates with areas on the order of square meters and with complex shapes.[37,38] Therefore, ED of PbO_2 fulfills the low-cost and scale-up requirements. On the other hand, conversion of PbI_2[39] or postdeposition processing of $MAPbI_3$[40] with CH_3NH_3I vapor yields uniform perovskite films with a low grain boundary density, concurrently maintaining a reasonable processing cost. Furthermore, to the best of our knowledge, this work is the first to describe the conversion of a PbO_2 film into a PbI_2 film by HI vapor as well as the reactor design necessary for such a conversion. PbI_2 film fabrication methods are important because PbI_2 films serve as precursors for several halide perovskites, such as $HC(NH_2)_2PbI_3$ ($FAPbI_3$)[41] and others.[42]

RESULTS AND DISCUSSION

Film Uniformity. In perovskite solar cells, deviations from the optimal perovskite film thickness can decrease the performance either by reducing absorption or by extending the path the charge carriers need to traverse before collection. In the literature, perovskite thickness uniformity is typically assessed from SEM images of film cross sections recorded on a scale of a few micrometers. However, Liu et al.[17] highlighted the disadvantages of this approach, demonstrating that spin-coated $MAPbI_{3-x}Cl_x$ films that are uniform on a scale of a few micrometers reveal thickness variations of ±100% from the mean thickness on a larger scale. Herein, the thickness uniformity of the films was evaluated by thickness measurements at five distinct points across every film. Four measurement points were located at an equal distance from the two nearest deposition area borders, whereas the fifth one was located in the middle of the deposition area (Figure 1a).

ED of PbO_2 Films. Anodic ED of PbO_2 proceeds according to reaction 1.

$$Pb^{2+}(aq) + 2H_2O(l) \rightarrow PbO_2(s) + 4H^+(aq) + 2e^- \quad (1)$$

The color of the electrodeposited PbO_2 changed from beige to dark red with increasing film thickness. The film thickness becomes less uniform with increasing current density (Figure 1b). Increased current density causes the reactants to deplete in the vicinity of the substrate, allowing variations in the diffusion fluxes between the substrate edges and its center area to affect the uniformity of the coating.[43] In the case of PbO_2 deposition, an excessively low current density leads to an impractically low growth rate. A sufficient growth rate and very uniform PbO_2

DOI: 10.1021/acsomega.6b00351
ACS Omega 2016, 1, 1296−1306

films are obtained at 0.25 mA cm^{-2}. In addition, at 0.25 mA cm^{-2}, the current distribution and film uniformity are governed by the geometry of the bath. Rotating the substrate by 45° with respect to its normal face-to-face orientation with the counter electrode alters the thickness profile of the deposited film and produces thinner PbO_2 film in the area further from the counter electrode (Table 1, compare films A and B, see also Figure S1). Such a behavior suggests that proper optimization of the bath geometry can further improve the film uniformity. Uniformity of the PbO_2 film is important because it is retained through the vapor conversion steps into the final $MAPbI_3$ film.

Table 1. Thicknesses of Electrodeposited PbO_2 Films[a]

	thickness (nm)			
	acetate bath (this work)			nitrate bath[32]
measured from	film A	film B	film C	film D
P1	53	58	98	109
P2	53	51	101	108
P3	47	42	88	79
P4	46	43	89	85
P5	46	40	92	83
mean	49	47	94	93
σ_{rel}	7%	16%	6%	16%

[a]Films A and B deposited at 0.25 mA cm^{-2} for 200 s. Film A deposited with the substrate surface parallel and B, with the substrate surface at 45° with respect to the counter electrode surface. P1 and P4 of film B were located on the substrate edge closest to the counter electrode. C was deposited at 0.25 mA cm^{-2} for 375 s, whereas D was deposited at 1.8 V for 30 s. Both C and D were deposited with the substrate surface parallel to the counter electrode surface. A–C were deposited in a 0.1 M $Pb(CH_3COO)_2$, 1.0 M $Na(CH_3COO)$ bath, whereas D was deposited in a 0.1 M $Pb(CH_3COO)_2$, 0.2 M $NaNO_3$, 0.1 M HNO_3 bath.[32] Figures illustrating the thickness profiles of the films and bath geometries are available in the Supporting Information (Figures S1 and S2). Positions of measurement points P1–5 are shown in Figure 1a.

All PbO_2 films consist of grains of size 26 ± 11 nm (Figure 2a), which form larger agglomerates (Figure 2e). These agglomerates expand as the deposition proceeds and merge to form dense films (Figure 2b,c) with uniform coverage. The roughness of the films is affected by the size and shape of the agglomerates, for example, the root-mean-square (rms) roughness of a PbO_2 film deposited for 725 s is 33 nm, which is 18% of the film thickness. Macroscopically, full coverage is displayed by all of the PbO_2 films (Figure 2d,f). However, only the films deposited for 500 s or longer exhibit full coverage on a microscopic scale (Figure 2c), whereas in the films deposited for shorter periods, areas with an exposed FTO surface are observed (Figure 2e). Despite this lack of full coverage in thinner films, the amount of PbO_2 deposited depends linearly on the deposition time, and the growth rate is 0.25 ± 0.01 nm s^{-1} (Figure 1c). In contrast, there is no correlation between deposition time and thickness nonuniformity. The thickness nonuniformity in the films is ≤9%.

The as-deposited PbO_2 films contain a mixture of orthorhombic α-PbO_2 and tetragonal β-PbO_2 phases (Figure 1d). The ratio of these phases was impossible to determine due to the broadness of the X-ray diffraction (XRD) reflections. Therefore, the mean density (9.71 g cm^{-3}) of the α- and β-phases (9.87 and 9.55 g cm^{-3}, respectively) was used for the thickness calculations. XRD reflections appear to broaden due to the small size of the grains, as observed with AFM and FESEM. According to the X-ray diffractograms measured with the θ–2θ geometry, these grains do not exhibit a preferential orientation.

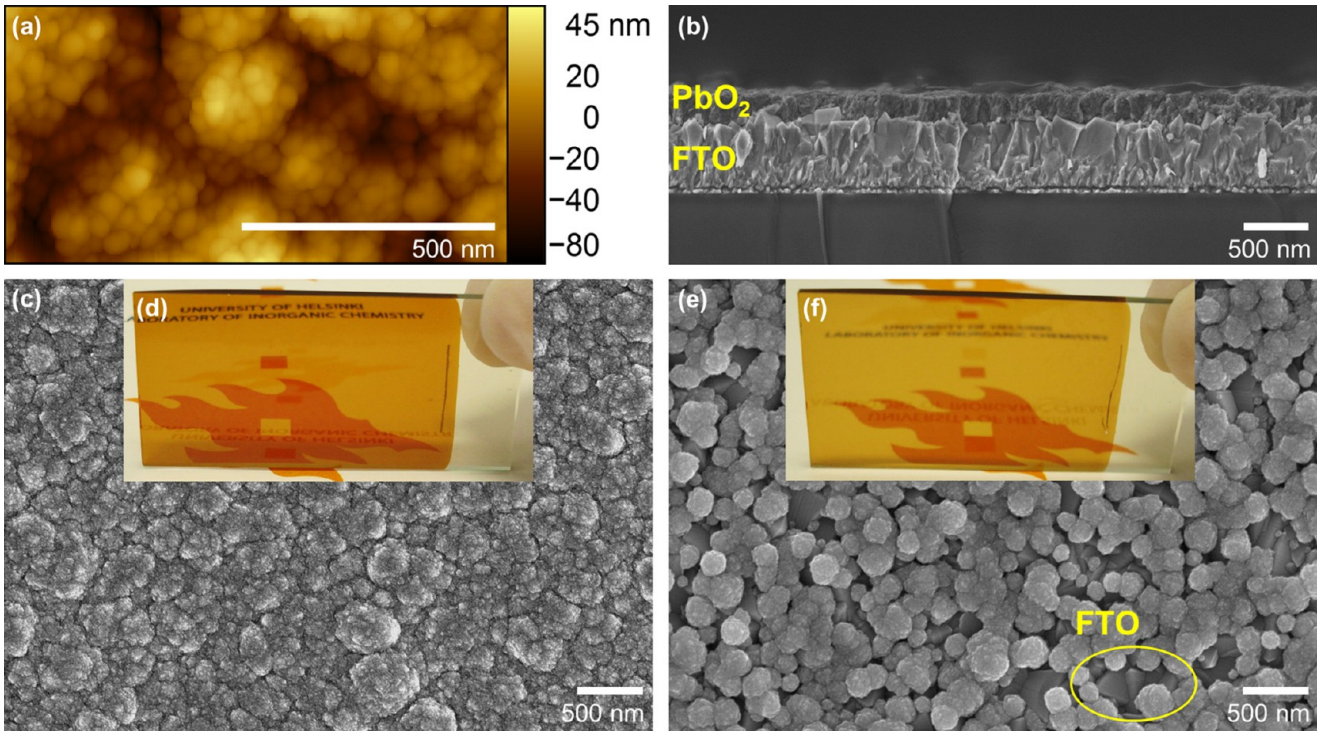

Figure 2. (a) Atomic force microscopy (AFM) image, (b) cross-sectional and (c) top-view field emission scanning electron microscopy (FESEM) images, and (d) a photograph of a PbO_2 film deposited at 0.25 mA cm^{-2} for 725 s. (e) FESEM image and (f) a photograph of a PbO_2 film deposited at 0.25 mA cm^{-2} for 400 s. The outlined area in (e) is the exposed FTO surface.

DOI: 10.1021/acsomega.6b00351
ACS Omega 2016, 1, 1296–1306

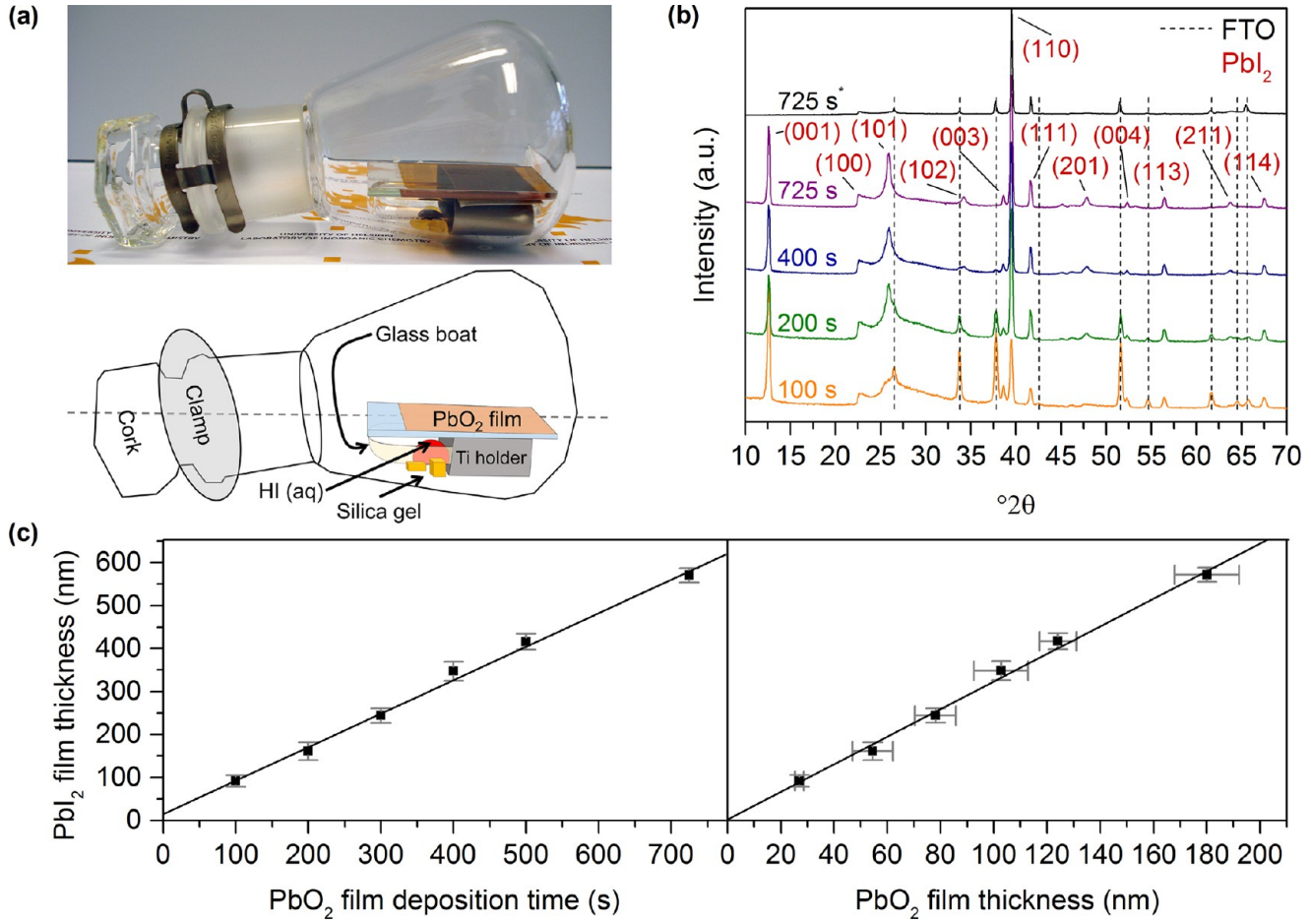

Figure 3. (a) Photograph and schematic picture of the reactor assembly for converting PbO_2 films into PbI_2 films. (b) X-ray diffractograms of PbI_2 films obtained by the conversion of PbO_2 films deposited for different times. The topmost diffractogram denoted by an asterisk was measured with the θ–2θ geometry, whereas other diffractograms were measured with a grazing incidence geometry. (c) PbI_2 film thickness as a function of the PbO_2 deposition time and PbO_2 film thickness. R^2 is 0.996 for the fitted curve on the left-hand-side graph and 0.995 for the one on the right-hand-side graph.

PbO_2 films display an optical band gap of 1.4 ± 0.1 eV. This value is in agreement with the values reported previously for PbO_2.[44,45] The EDX spectra revealed no impurities, and all of the films passed the Scotch tape adhesion test without delaminating. No delamination occurred even in the case of films grown for 5100 s, whose thickness, estimated from the growth rate (Figure 1c), is 1.3 μm.

In the literature, perovskite films have been made starting from electrodeposited lead monoxide (PbO) that is converted to PbI_2 or directly to $MAPbI_3$.[46,47] However, ED of PbO requires unstable H_2O_2-containing solutions or additionally dimethyl sulfoxide, elevated temperature, and solution degassing to remove dissolved O_2. In contrast, PbO_2 ED does not require solution degassing and proceeds under ambient conditions in a stable aqueous solution. The acetate-based ED solution employed in this study results in a lower growth rate than that of the nitrate-containing solution used by Chen et al.[32] On the other hand, the acetate solution produces more uniform films (compare films C and D in Table 1, see also Figure S2), and the lower growth rate enables more precise thickness control. Further comparison of ED-based processes for $MAPbI_3$ films is provided in Table S1.

Conversion of PbO_2 Films into PbI_2. The electrodeposited PbO_2 films were converted into PbI_2 films by exposing them to an excess of HI vapor, which, to the best of our knowledge, has not been reported elsewhere. The conversion occurs only at an elevated temperature; therefore, removing the reactor from the heat source too early will quench the conversion process and produce partially converted films. The iodine content of a set of partially converted PbO_2 films (Figure S3) and their phase compositions (Figure S4) suggest that for PbO_2 films deposited for 725 s or less, the conversion is completed in 90 min. The use of a glass reactor (Figure 3a) also allows us to visually observe the progress of the conversion (see Video S1). The appearance of the film changes during the conversion, due to changes in the band gap and roughness, which translate into changes in the reflectance and transmittance (see Figure S5 for UV–vis transmittance of as-deposited, partially converted, and fully converted films). Therefore, an indication of the completion of the conversion can be obtained from the lack of further changes in the color of the film. During the conversion, the reaction front advances from the edges of the PbO_2 film toward its center. The reaction appears to involve PbO_2 reduction by iodide (eq 2). The XRD patterns of the partially converted films (Figure S4) additionally suggest that this reaction may proceed through the PbI(OH) intermediate (eqs 3 and 4).

$$PbO_2(s) + 4HI(g) \rightarrow PbI_2(s) + I_2(g) + 2H_2O(g) \quad (2)$$

DOI: 10.1021/acsomega.6b00351
ACS Omega 2016, 1, 1296–1306

$$PbO_2(s) + 3HI(g) \rightarrow PbI(OH)(s) + I_2(g) + H_2O(g) \quad (3)$$

$$PbI(OH)(s) + HI(g) \rightarrow PbI_2(s) + H_2O(g) \quad (4)$$

Pb^{4+} in PbO_2 is a hard Lewis acid and is easily reduced because the inert pair effect makes the lead +II oxidation state more stable than the +IV oxidation state. Iodide, a soft Lewis base, in accordance with the Lewis hard−soft acid−base principle, binds preferably to Pb(II), which is a soft Lewis acid.

Initial conversion experiments without silica gel revealed that the formed PbI_2 film is sensitive to humidity during conversion. As the conversion proceeds, water droplets may condense on the reactor walls and substrate. These droplets, upon contact, degrade the formed PbI_2 film. The film appears to dissolve in the droplets. The droplet condensation ceases when the reactor contains silica gel granules. The granules absorb moisture originating from the hydroiodic acid. The amount of hydroiodic acid needs to be optimized for different PbO_2 film thicknesses and reactor volumes (Table 2). Even if reaction 2 liberates water as well, the main concern is water evaporating from hydroiodic acid. Therefore, if the conversion was performed with HI gas, silica gel would hardly be needed.

Table 2. Volumes of Hydroiodic Acid Used for the Conversion of PbO_2 Films

PbO_2 film		hydroiodic acid (μL)	
deposition time (s)	thickness (nm)	50 mL reactor	100 mL reactor
100	28 ± 2	20	30
200	54 ± 8	20	30
300	78 ± 8		40
400	103 ± 10	40	40
500	124 ± 7		60
725	180 ± 12	60	80
5100	1275[a]		300

[a]Thickness estimated from the growth rate (Figure 1c); the thickest film was converted to PbI_2 in 4 h.

X-ray diffractograms of the converted films lack PbO_2 reflections (see Figure S6), whereas reflections characteristic to crystalline PbI_2 emerge (Figure 3b). PbI_2 crystallites orient in the films primarily with the (110) planes parallel to the surface (Figure 3b). Similar orientation is observed in PbI_2 films made by converting electrodeposited PbO_2 films in solution; however, (001) planes are predominantly parallel to the film surface in spin-coated PbI_2.[32] PbI_2 has a two-dimensional layered structure, in which bonding between the layers is only due to weak interactions. These layers and interlayer gaps lie perpendicular to the film surface when (110) planes are parallel to the surface (see Figure S7). Consequently, the interlayer gaps extend through the film thickness, and in the subsequent conversion step to the perovskite, they may act as transport paths for the conversion reagent molecules.

PbI_2 is less dense (ρ = 6.10 g cm^{-3}) than PbO_2 (ρ = 9.6−9.9 g cm^{-3}); therefore, upon conversion, the volume of the PbO_2 grains should expand. In theory, if the grains would expand only perpendicular to the film surface, the film thickness (d) would increase by a factor of 3 (eq 5).

$$d_{PbI_2} = \rho_{PbO_2} M_{PbI_2} / \rho_{PbI_2} M_{PbO_2} d_{PbO_2} = 3.07 d_{PbO_2} \quad (5)$$

A similar factor of 3.20 ± 0.10 is obtained experimentally from the PbI_2 versus PbO_2 film thickness plot (Figure 3c). Furthermore, PbI_2 film thickness plotted against PbO_2 film deposition time reveals that the effective growth rate of PbI_2 films is 0.78 ± 0.02 nm/s. PbI_2 films demonstrate relative thickness variations of ≤8% across the film. This value is correlated with the thickness variations in PbO_2 films, implying that the thickness profile (see films A and C from Table 1 and Figures S1 and S2) is retained on conversion. Examination of the PbI_2 film morphology reveals that during the conversion the grains also show slight lateral growth. The lateral growth explains the pinhole sealing in the PbI_2 films converted from the PbO_2 films deposited for 400 s (compare Figures 2e and 4a). The lateral growth is favorable because it compensates for the defects in the PbO_2 films and promotes the formation of dense PbI_2 films (Figure 4c). Pinholes still occur in PbI_2 films converted from PbO_2 films deposited for ≤200 s. All PbI_2 films appear macroscopically uniform (Figure 4d), whereas on a smaller scale, they consist of grains with different sizes (Figure 4a,b). The grain size seems to increase with increasing film thickness. For example, in the PbI_2 films converted from PbO_2 deposited for 725 s, the grain size is 0.33 ± 0.13 μm. This grain size is about 10 times larger than that of the original PbO_2 film and can be correlated to the more than doubled roughness (rms 79 nm) of the converted film. The roughness is, however, 14% of the PbI_2 film thickness, suggesting in relative terms that the surface has leveled a bit. PbI_2 films are yellow, translucent, and display an optical band gap of 2.4 ± 0.1 eV, which agrees with the value previously reported for PbI_2.[48]

Conversion of PbI_2 Films into $CH_3NH_3PbI_3$. The PbI_2 films made by conversion of electrodeposited PbO_2 films were finally converted into $MAPbI_3$ films by exposing them to CH_3NH_3I vapor. Conversion to $MAPbI_3$ proceeds in a reactor analogous to the reactor used for the conversion of PbO_2 to PbI_2 (see Figure S8). Conversion in an inert atmosphere (N_2 or Ar) leads to film deterioration, whereas conversion in static vacuum yields $MAPbI_3$ films (see Video S2) as desired. According to EDX, the films contain lead and iodine in amounts in agreement with the stoichiometry of $MAPbI_3$ (Figure 5a). Furthermore, the EDX spectra of the films contain nitrogen and carbon signals, but the limitations of EDX do not allow quantification of these light elements. No impurity elements were observed in the EDX spectra, and no PbI_2 reflections are observed in the XRD patterns of the films (see Figure S6 for comparison of the film diffractograms at different steps). If the conversion process is interrupted too early, PbI_2 reflections are still observed in the X-ray diffractograms of the partially converted films (Figure S9). The iodine content in the films increases linearly with time during the conversion to a level corresponding to that of $MAPbI_3$ (Figure S10) and remains constant thereafter. Because the thicknesses of the PbI_2 films are known, extrapolating the iodine content increase to a constant level and assuming that this increase is proportional to the conversion rate allow us to estimate the latter. The conversion rate determined with these assumptions is ca. 1.1 μm of the PbI_2 film thickness per hour. The completion of the conversion of PbI_2 to $MAPbI_3$ can also be detected by the absence of further changes in the appearance of the film. These changes in the appearance are due to the changes in the optical properties such as transmittance (Figure S11) of the film. Recently, Brenner et al. suggested that at elevated temperature the reaction of PbI_2 with CH_3NH_3I and the formation of $MAPbI_3$ proceed by a deconstruction−reconstruction mechanism.[49]

DOI: 10.1021/acsomega.6b00351
ACS Omega 2016, 1, 1296−1306

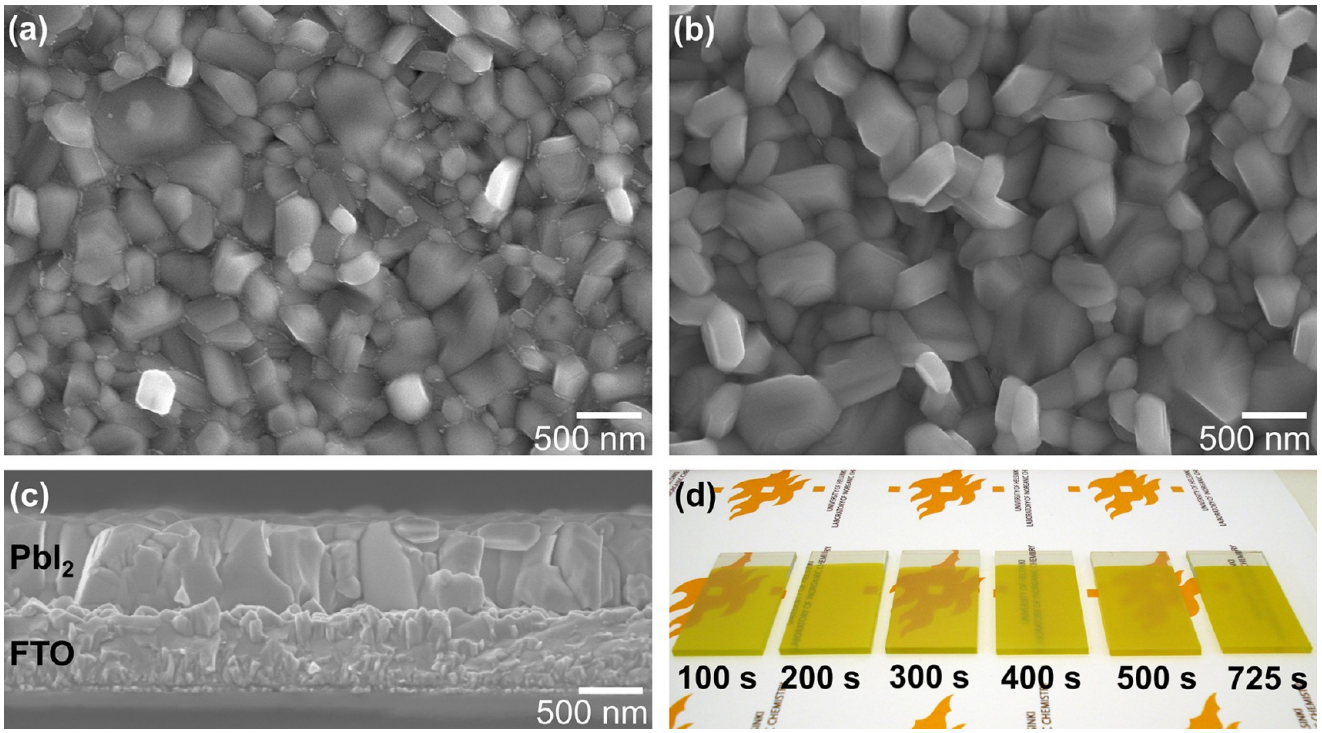

Figure 4. FESEM images of PbI_2 films prepared by converting PbO_2 films deposited for (a) 400 s and (b, c) 725 s. (d) Photograph of PbI_2 films prepared by converting PbO_2 films electrodeposited for 100−725 s.

Controlling the duration of the conversion allows the preparation of different crystal phases of $MAPbI_3$. $MAPbI_3$ films crystallize in the tetragonal β-phase (Figure 5b) when the conversion lasts for 2 h. In contrast, if the conversion is continued for 24 h, the resulting films have a pseudocubic α-phase (Figure 5b). β-$MAPbI_3$ is known to exhibit a phase transition to the α-phase at an elevated temperature.[50] Therefore, prolonged annealing after the conversion process is complete induces the β- to α-phase transition, and rapid removal of the reactor from the heat source prevents the reverse transition and yields α-phase films. The α-phase is less distorted from the ideal perovskite structure and is more compact compared with the β-phase. Such compactness can be beneficial to the stability of the perovskite. For instance, in the case of $MAPbI_{3-x}Br_x$ solid solutions, phase transition to the pseudocubic phase decreased the moisture sensitivity of the perovskite.[10] For $MAPbI_3$ perovskite, Milot et al.[51] reported that upon temperature increase and phase transition to the pseudocubic phase the rate constant for Auger recombination decreases. The Auger recombination rate is an essential parameter for devices with large charge-carrier densities, such as lasers and concentrated photovoltaics. Furthermore, photovoltaic devices with pseudocubic $MAPbI_3$ exhibit less hysteretic behavior, in contrast to devices with the tetragonal phase.[52] For films of either of the phases, XRD measurements with the θ−2θ geometry revealed no significant preferential orientation.

There appears to be no limit to the maximum convertible PbI_2 thickness. Even 10 μm thick $MAPbI_3$ films (Figure 6a) could be produced provided that the duration of conversion was long enough (24 h). One conversion of such thick film was interrupted at 2 h, and the cross section of this film revealed two distinct layers (Figure 6b). The contrast difference suggests that the topmost layer is $MAPbI_3$, whereas the layer underneath is unconverted PbI_2. The presence of PbI_2 is also indicated by PbI_2 reflections in the X-ray diffractogram of this film. The interrupted conversion allows us to evaluate the conversion rate by measuring the geometric thicknesses of the PbI_2 and $MAPbI_3$ layers from the film cross section. The rate is ca. 1.1 μm/h with respect to the thickness of the converted PbI_2 or 2 μm/h with respect to the thickness of the formed $MAPbI_3$ film, in agreement with the rate determined from the change in the iodine content in the films.

$MAPbI_3$ films should be thicker than the PbI_2 and PbO_2 films from which they were prepared because the $MAPbI_3$ phases are less dense (ρ_α = 4.09 and ρ_β = 4.16 g cm^{-3}) than PbI_2 or PbO_2. The thickness increase factor for the β-$MAPbI_3$ films obtained by an approach similar to the one in eq 1 is 1.97 with respect to that of PbI_2 and 6.06 with respect to that of PbO_2. The experimental factors, that is, 1.84 ± 0.04 with respect to that of PbI_2 (Figure 5c) and 5.84 ± 0.09 with respect to that of PbO_2, agree with the predicted thickness increase. The $MAPbI_3$ film thickness exhibits a linear dependence on the deposition time of the original PbO_2 film (Figure 5c), and the $MAPbI_3$ growth rate with respect to the PbO_2 deposition time is 1.42 ± 0.03 nm/s. The linear dependence implies that the $MAPbI_3$ film thickness can be conveniently and accurately controlled by the PbO_2 ED time. The deposition time and thus the final $MAPbI_3$ thickness have no effect on the uniformity. The relative thickness nonuniformity of the $MAPbI_3$ films is 8.5%, a value markedly similar to the nonuniformities of the PbI_2 and PbO_2 films. The similarity suggests that $MAPbI_3$ inherits its thickness profile from the initial PbO_2 film, and this in turn explicitly demonstrates the significance of the PbO_2 uniformity. As discussed previously, the PbO_2 film uniformity could be improved by optimizing the ED bath geometry or alternatively by employing suitable bath additives.

$MAPbI_3$ films are black in color with metal-like reflective surfaces (Figure 7a,b). The surface roughness of the β-phase

DOI: 10.1021/acsomega.6b00351
ACS Omega 2016, 1, 1296−1306

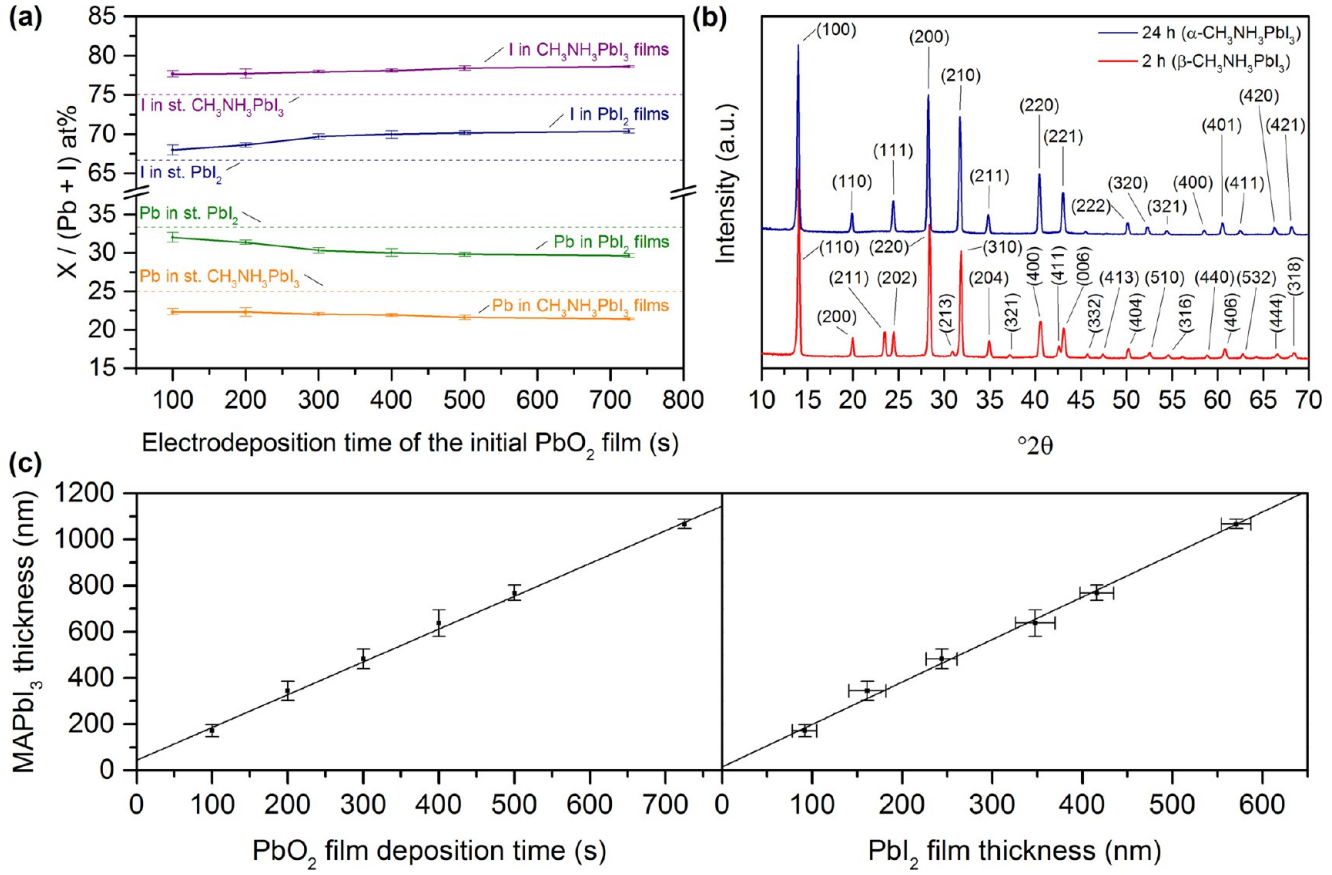

Figure 5. (a) Pb/(Pb + I) and I/(Pb + I) atom percent (atom %) ratios in $MAPbI_3$ films. For comparison, the same ratios are shown for PbI_2 films, and the ratios for stoichiometric compounds (st.) are indicated by dashed lines. (b) Grazing incidence X-ray diffractograms of $MAPbI_3$ films prepared by 24 and 2 h long conversions. Both films originate from PbO_2 film deposited for 725 s. The reflections are indexed according to single-crystal data from Stoumpos et al.[50] (c) $MAPbI_3$ film thickness as a function of PbO_2 deposition time and PbI_2 film thickness. R^2 = 0.998 for fitted curve of both the left- and right-hand-side graphs.

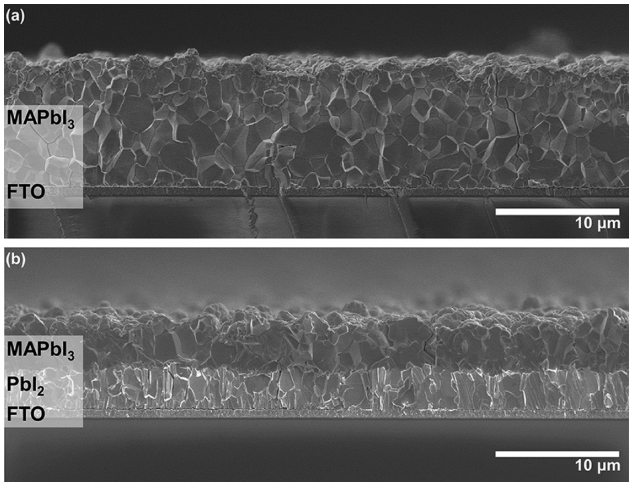

Figure 6. Cross-sectional FESEM images of $MAPbI_3$ films obtained by converting PbI_2 films for (a) 24 h and (b) 2 h. Both (a) and (b) samples originate from PbO_2 deposited for 5100 s.

films originating from the PbO_2 films deposited for 725 s is 78 nm (rms), and these films consist of grains of size 0.30 ± 0.12 μm. This grain size is similar to that of the preceding PbI_2 film converted from the PbO_2 film deposited for 725 s. In contrast to the β-phase films, the α-phase films originating from the PbO_2 films deposited for 725 s are smoother, with a surface roughness of 69 nm (rms), and consist of larger grains (size 0.55 ± 0.12 μm). A larger grain size is beneficial for the efficiency of perovskite-based devices, such as LEDs, TFTs, ReRAMs, and photovoltaic devices, as it translates to a lower grain boundary density, improving the charge transfer properties.[3,7,22,40,53−55] In addition, a lower grain boundary density should retard hydration and decomposition of the perovskite because grain boundaries facilitate transport of water molecules within the perovskite.[56,57] The conversion of PbI_2 to $MAPbI_3$ leveled the films, similar to the conversion of PbO_2 to PbI_2; for instance, the rms roughness is 7% of the film thickness for the β-$MAPbI_3$ film originating from the PbO_2 film deposited for 725 s and 6% for the α-$MAPbI_3$ film originating from a similar PbO_2 film.

Markedly, the voids have been sealed even in the thinnest $MAPbI_3$ films originating from PbO_2 films deposited for 100 s (Figure 7d). The tendency for such self-sealing is an advantage of the vapor conversion method, as it allows some imperfections in the intermediate PbI_2 and PbO_2 films without compromising the capability to produce continuous $MAPbI_3$ films, at least in the examined thickness range (0.1−10 μm).

According to UV−vis measurements, both α- and β-$MAPbI_3$ films exhibit an optical band gap of 1.6 ± 0.1 eV. These values agree with the values previously reported for these $MAPbI_3$ phases.[10,50,51] Furthermore, $MAPbI_3$ films behave as photoconductors according to *I*−*V* measurements (Figure S12). A potential difference of 0.9 V was measured between the FTO

DOI: 10.1021/acsomega.6b00351
ACS Omega 2016, 1, 1296−1306

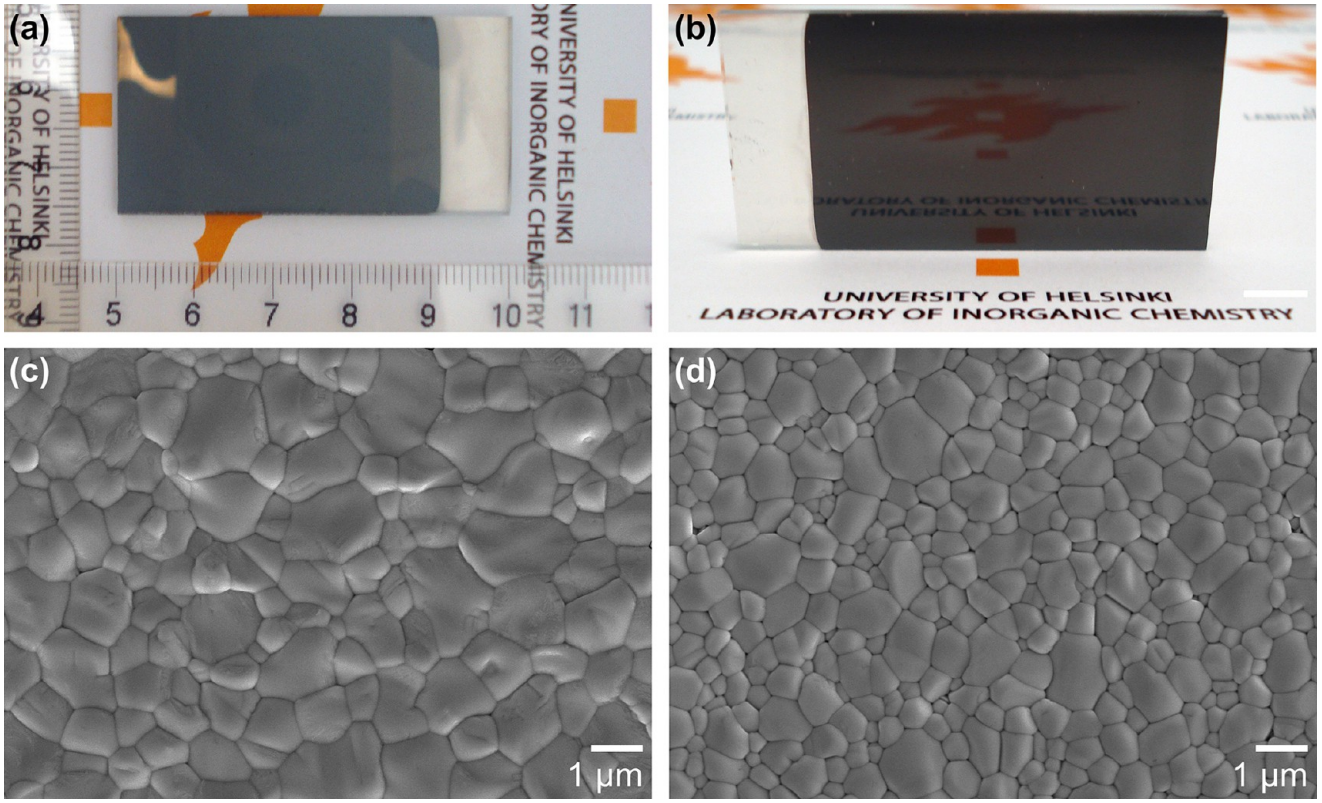

Figure 7. Photograph of $MAPbI_3$ films originating from PbO_2 films deposited for 725 s (a) and 400 s (b), as well as FESEM images of $MAPbI_3$ films originating from PbO_2 films deposited for 725 s (c) and 100 s (d). The conversion duration to $MAPbI_3$ was 2 h.

bottom contact and the In−Ga eutectic top contact of the 1.1 μm β-$MAPbI_3$ film when it was illuminated with 1000 W m^{-2} as opposed to zero potential difference measured without illumination. These observations indicate that the $MAPbI_3$ films made by vapor conversion of electrodeposited PbO_2 are photoactive.

Our preliminary results indicate that PbI_2 films react also with $HC(NH_2)_2I$ (formamidinium iodide (FAI)) under the same conditions as their reaction with CH_3NH_3I. However, the conversion process is much slower with FAI, and even after 24 h, a minor reflection at 12.4°2θ, indicative of unreacted PbI_2, is observed in the X-ray diffractogram of the film (Figure S13).

CONCLUSIONS

Uniform $MAPbI_3$ films are reproducibly prepared by ED together with a two-step vapor conversion. Grain growth during the vapor conversion steps mitigates microscopic voids in the films to some extent, improving the quality of the final $MAPbI_3$ film. The crystal phase of the $MAPbI_3$ film as well as its grain size can be adjusted by changing the duration of the second vapor conversion step, whereas adjusting the ED duration allows simple control over the film thickness. A wide range of $MAPbI_3$ film thicknesses, from tens of nanometers to tens of micrometers, is accessible with the described approach. ED lacks an inherent substrate size limit and is scalable in a roll-to-roll or brush manner or to large batches, whereas vapor exposure steps are in principle limited only by the reaction vessel size. Together, the qualities of this approach make it a promising deposition method for a wide range of perovskite film applications, such as LEDs, TFTs, ReRAM, photodetectors, and photovoltaics. Future work may focus on further upscaling of the method. Alternatively, further simplification of the PbO_2 to PbI_2 conversion step by exploiting gaseous hydrogen iodide may be explored.

MATERIALS AND METHODS

Substrate Preparation. TEC 7 fluorine-doped tin dioxide-coated glass substrates (FTO) were obtained from SOLEMS. Before ED, the substrates were rinsed with ethanol, dried with compressed air, and annealed in an air oven at 350 °C for 2 h. The heating rate was 3 °C/min.

ED of PbO_2 Films. An aqueous solution containing 0.10 M lead(II) acetate trihydrate (Sigma-Aldrich, 99%) and 1.00 M sodium acetate (Sigma-Aldrich, 99%) served as an ED bath for PbO_2 films.[58] The solution was prepared by first dissolving sodium acetate, followed by initial pH adjustment to 5.6−5.8. Next, lead(II) acetate trihydrate was dissolved, followed by final pH adjustment to 5.5. The pH adjustments were done with 5 M acetic acid and 3 M sodium hydroxide. The solutions were prepared using 18 MΩ cm resistivity water from a Millipore Milli-Q system.

ED was performed without stirring at ambient temperature with an Autolab PGSTAT20 potentiostat−galvanostat and a three-electrode arrangement. FTO slides (5.0 × 2.5 cm^2) acted as working electrodes, with the active deposition area being 10 cm^2 (4.0 × 2.5 cm^2). A cylinder-shaped platinum net (r = 1.5 cm, h = 3.7 cm) was used as the counter electrode and an Ag/AgCl/KCl (3 M) electrode as the reference electrode. EDs were done galvanostatically at a current density of 0.25 mA cm^{-2} unless specified otherwise.

Conversion of PbO_2 to PbI_2. Conversion of the as-deposited PbO_2 to PbI_2 was carried out in a 100 mL Erlenmeyer flask with a ground-glass joint (VWR, 29/32). Hydroiodic acid (20−300 μL, 55%, no stabilizer; Sigma-

DOI: 10.1021/acsomega.6b00351
ACS Omega 2016, 1, 1296−1306

Aldrich) was pipetted into a glass boat (l = 5 cm, w = 1 cm), and the boat was transferred into the flask. A total of 250 mg of silica gel granules (2−6 mm; VWR Chemicals) was spread around the boat inside the flask to absorb excess water from the hydroiodic acid. A substrate holder was bent from a titanium foil (Alfa Aesar, 0.25 mm, 99.5%) and placed over the boat. The PbO_2 films were placed onto the holder facing upward. The flask was then flushed with nitrogen (99.999%) for 2 min and sealed with a glass stopper. A pinch clamp and high-vacuum silicone grease were used to ensure hermetic seal. The assembly was heated in either a stirred oil bath or an air oven and kept at 90 °C for 90 min unless otherwise specified. After conversion, the PbI_2 films were removed from the still hot flask.

Conversion of PbI_2 to $CH_3NH_3PbI_3$. CH_3NH_3I was synthesized by adding hydroiodic acid (55%, no stabilizer; Sigma-Aldrich) dropwise to a methylamine solution (TCI, 40% in methanol) that was stirred and kept in an ice-bath. Methanol and water were evaporated with a rotary evaporator, leaving yellow crystals of the raw compound. The raw compound was recrystallized in ethanol. The resulting white crystals were separated by filtering, washed with tetrahydrofuran as well as diethyl ether, and then dried. Dry CH_3NH_3I was kept in a N_2 glovebox (<0.5 ppm of O_2 and H_2O).[54]

Conversion of PbI_2 to $MAPbI_3$ was carried out in an assembly similar to the one used for the PbO_2 to PbI_2 conversion, with stopcock adapter instead of glass stopper. No silica gel was used, and the boat was loaded with 100 mg of CH_3NH_3I instead of hydroiodic acid. The flask was evacuated with a rotary pump to a pressure of 0.9 mbar before heating to 180 °C by means of either a stirred oil bath or an air oven. Unless otherwise stated, the flask was kept at 180 °C for 2 h. To avoid CH_3NH_3I condensation, the $MAPbI_3$ films were taken out of the flask immediately after the flask was removed from the hot oil or oven.

Characterization. The morphology of the films was studied by FESEM using a Hitachi S-4800 instrument. The composition of the films was studied by energy-dispersive X-ray (EDX) spectroscopy with an Oxford INCA 350 energy spectrometer connected to the FESEM instrument. The films thicknesses were calculated from the EDX data with GMRFilm software[59] using bulk densities. All of the reported thicknesses are mean values of five measurements from distinct positions across the film. The thickness errors are standard deviations of these five measurements.

AFM images for analyzing the surface roughness and morphology were recorded using a Veeco Multimode V AFM with a Nanoscope V controller. The images were captured in the tapping mode (intermittent contact mode) in air using silicon probes, with a nominal tip radius of 8 nm and a nominal spring constant of 40 N/m (RTESP from Bruker). Image analysis was performed with Gwyddion software.[60]The images were plane-fitted to remove artifacts caused by sample tilt and scanner bow. Roughness was calculated as an rms value (or Rq) from 5 × 5 μm^2 images for all films. For grain size evaluation, grains were identified by a watershed algorithm from 5 × 5 μm^2 images for PbI_2 and $MAPbI_3$ films, whereas for PbO_2 films, 0.5 × 0.5 μm^2 images were used due to the small size of the grains. The grain size was calculated as the median diameter of circles with areas equivalent to the area of the identified grains.

The crystallinity of the film was studied with a PANalytical X'Pert Pro MPD diffractometer using Cu Kα-radiation. XRD patterns were measured using both grazing incidence (GIXRD, incident angle 1°) and θ−2θ geometries. Transmittance measurements in the UV−vis range were performed with a Hitachi U2000 spectrophotometer. Optical band gaps were evaluated from the transmittance data and Tauc plots according to the approach described in the literature.[61,62] The band gaps of PbI_2 and $MAPbI_3$ were assumed to be direct-allowed and that of PbO_2 indirect-allowed.

I−V measurements were carried out with a Keithley 2400 Source Meter, using a step width of 0.05 V and a source step delay of 0.1 s. Electrical contacts were made by applying Ga−In eutectic alloy (Sigma-Aldrich) dots (ca. 3 mm^2) to FTO and $MAPbI_3$ and contacting these dots with needle probes. A halogen spot lamp (50 W) was used for illumination.

■ ASSOCIATED CONTENT

Supporting Information

The Supporting Information is available free of charge on the ACS Publications website at DOI: 10.1021/acsomega.6b00351.

Two different PbO_2 ED bath geometries and their effect on PbO_2 the film thickness profile (Figure S1); comparison of PbO_2 film thickness profiles obtained from different ED baths (Figure S2); comparison of ED-based processes for MAPbI3 films reported in the literature and in this work (Table S1); iodine content in the films at different stages of the PbO_2 to PbI_2 conversion (Figure S3); X-ray diffractograms of the films at different stages of the PbO_2 to PbI_2 conversion (Figure S4); UV−vis transmittance of the films at different stages of the PbO_2 to PbI_2 conversion (Figure S5); comparison of X-ray diffractograms of the as-deposited PbO_2 film, the PbO_2 film converted to the PbI_2 film, and the PbI_2 film converted to the $MAPbI_3$ film (Figure S6); crystal structure of PbI_2 with (001) and (110) planes visualized (Figure S7); photograph of the reactor used for converting PbI_2 films into $MAPbI_3$ (Figure S8); X-ray diffractograms of the films at different stages of the PbI_2 to $MAPbI_3$ conversion (Figure S9); iodine content in the films at different stages of the PbI_2 to $MAPbI_3$ conversion (Figure S10); UV−vis transmittance of the films at different stages of the PbI_2 to $MAPbI_3$ conversion (Figure S11); I−V curves of the β-$MAPbI_3$ film with and without illumination and the setup used for electrical measurements (Figure S12); X-ray diffractogram of the PbI_2 film converted with FAI and its FESEM image (Figure S13) (PDF)

Recorded conversion of an electrodeposited PbO_2 film (at 0.25 mA cm^{-2} for 100 s) into PbI_2 (Video S1) (MPG)

Recorded conversion of a PbI_2 film into $MAPbI_3$. The PbI_2 film was obtained by converting the PbO_2 film electrodeposited at 0.25 mA cm^{-2} for 725 s (Video S2) (MPG)

■ AUTHOR INFORMATION

Corresponding Author

*E-mail: georgi.popov@helsinki.fi.

ORCID

Georgi Popov: 0000-0003-1233-8327

Marianna L. Kemell: 0000-0002-3583-2064

Author Contributions

The manuscript was written through contributions of all authors. All authors have given approval to the final version of the manuscript.

DOI: 10.1021/acsomega.6b00351
ACS Omega 2016, 1, 1296−1306

Notes

The authors declare no competing financial interest.

■ ACKNOWLEDGMENTS

This work was supported by the Finnish Center of Excellence in Atomic Layer Deposition (ALDCoE), funded by the Academy of Finland and the doctoral program in Materials Research and Nanosciences (MATRENA) of the University of Helsinki.

■ REFERENCES

(1) Tan, Z.-K.; Moghaddam, R. S.; Lai, M. L.; Docampo, P.; Higler, R.; Deschler, F.; Price, M.; Sadhanala, A.; Pazos, L. M.; Credgington, D.; et al. Bright Light-Emitting Diodes Based on Organometal Halide Perovskite. *Nat. Nanotechnol.* **2014**, *9*, 687−692.

(2) Cho, H.; Jeong, S.-H.; Park, M.-H.; Kim, Y.-H.; Wolf, C.; Lee, C.-L.; Heo, J. H.; Sadhanala, A.; Myoung, N.; Yoo, S.; et al. Overcoming the Electroluminescence Efficiency Limitations of Perovskite Light-Emitting Diodes. *Science* **2015**, *350*, 1222−1225.

(3) Wu, Y.; Li, J.; Xu, J.; Du, Y.; Huang, L.; Ni, J.; Cai, H.; Zhang, J. Organic−Inorganic Hybrid $CH_3NH_3PbI_3$ Perovskite Materials as Channels in Thin-Film Field-Effect Transistors. *RSC Adv.* **2016**, *6*, 16243−16249.

(4) Deschler, F.; Price, M.; Pathak, S.; Klintberg, L. E.; Jarausch, D.; Higler, R.; Hüttner, S.; Leijtens, T.; Stranks, S. D.; Snaith, H. J.; et al. High Photoluminescence Efficiency and Optically Pumped Lasing in Solution-Processed Mixed Halide Perovskite Semiconductors. *J. Phys. Chem. Lett.* **2014**, *5*, 1421−1426.

(5) Moehl, T.; Im, J. H.; Lee, Y. H.; Domanski, K.; Giordano, F.; Zakeeruddin, S. M.; Dar, M. I.; Heiniger, L. P.; Nazeeruddin, M. K.; Park, N. G.; et al. Strong Photocurrent Amplification in Perovskite Solar Cells with a Porous TiO_2 Blocking Layer under Reverse Bias. *J. Phys. Chem. Lett.* **2014**, *5*, 3931−3936.

(6) Lin, Q.; Armin, A.; Burn, P. L.; Meredith, P. Filterless Narrowband Visible Photodetectors. *Nat. Photonics* **2015**, *9*, 687−694.

(7) Gu, C.; Lee, J.-S. Flexible Hybrid Organic−Inorganic Perovskite Memory. *ACS Nano* **2016**, *10*, 5413−5418.

(8) Chen, Y. S.; Manser, J. S.; Kamat, P. V. All Solution-Processed Lead Halide Perovskite-$BiVO_4$ Tandem Assembly for Photolytic Solar Fuels Production. *J. Am. Chem. Soc.* **2015**, *137*, 974−981.

(9) Green, M. A.; Emery, K.; Hishikawa, Y.; Warta, W.; Dunlop, E. D. Solar Cell Efficiency Tables (Version 47). *Prog. Photovoltaics* **2016**, *24*, 3−11.

(10) Noh, J. H.; Im, S. H.; Heo, J. H.; Mandal, T. N.; Seok, S. Il Chemical Management for Colorful, Efficient, and Stable Inorganic-Organic Hybrid Nanostructured Solar Cells. *Nano Lett.* **2013**, *13*, 1764−1769.

(11) Burschka, J.; Pellet, N.; Moon, S.-J.; Humphry-Baker, R.; Gao, P.; Nazeeruddin, M. K.; Grätzel, M. Sequential Deposition as a Route to High-Performance Perovskite-Sensitized Solar Cells. *Nature* **2013**, *499*, 316−319.

(12) Li, H.; Fu, K.; Hagfeldt, A.; Grätzel, M.; Mhaisalkar, S. G.; Grimsdale, A. C. A Simple 3,4-Ethylenedioxythiophene Based Hole-Transporting Material for Perovskite Solar Cells. *Angew. Chem., Int. Ed. Engl.* **2014**, *53*, 4085−4088.

(13) Mahmood, K.; Swain, B. S.; Amassian, A. Double-Layered ZnO Nanostructures for Efficient Perovskite Solar Cells. *Nanoscale* **2014**, *6*, 14674−14678.

(14) Mahmood, K.; Swain, B. S.; Kirmani, A. R.; Amassian, A. Highly Efficient Perovskite Solar Cells Based on a Nanostructured WO_3-TiO_2 Core-Shell Electron Transporting Material. *J. Mater. Chem. A* **2015**, *3*, 9051−9057.

(15) Peng, G.; Wu, J.; Wu, S.; Xu, X.; Ellis, J. E.; Xu, G.; Star, A.; Gao, D. Perovskite Solar Cells Based on Bottom-Fused TiO_2 Nanocones. *J. Mater. Chem. A* **2016**, *4*, 1520−1530.

(16) Huang, Y.; Wu, J.; Gao, D. High-Efficiency Perovskite Solar Cells Based on Anatase TiO_2 Nanotube Arrays. *Thin Solid Films* **2016**, *598*, 1−5.

(17) Liu, M.; Johnston, M. B.; Snaith, H. J. Efficient Planar Heterojunction Perovskite Solar Cells by Vapour Deposition. *Nature* **2013**, *501*, 395−398.

(18) Xiao, Z.; Bi, C.; Shao, Y.; Dong, Q.; Wang, Q.; Yuan, Y.; Wang, C.; Gao, Y.; Huang, J. Efficient, High Yield Perovskite Photovoltaic Devices Grown by Interdiffusion of Solution-Processed Precursor Stacking Layers. *Energy Environ. Sci.* **2014**, *7*, 2619−2623.

(19) Eperon, G. E.; Stranks, S. D.; Menelaou, C.; Johnston, M. B.; Herz, L. M.; Snaith, H. J. Formamidinium Lead Trihalide: A Broadly Tunable Perovskite for Efficient Planar Heterojunction Solar Cells. *Energy Environ. Sci.* **2014**, *7*, 982−988.

(20) Ahn, N.; Son, D. Y.; Jang, I. H.; Kang, S. M.; Choi, M.; Park, N. G. Highly Reproducible Perovskite Solar Cells with Average Efficiency of 18.3% and Best Efficiency of 19.7% Fabricated via Lewis Base Adduct of Lead(II) Iodide. *J. Am. Chem. Soc.* **2015**, *137*, 8696−8699.

(21) Yang, W. S.; Noh, J. H.; Jeon, N. J.; Kim, Y. C.; Ryu, S.; Seo, J.; Seok, S. Il High-Performance Photovoltaic Perovskite Layers Fabricated through Intramolecular Exchange. *Science* **2015**, *348*, 1234−1237.

(22) Sharenko, A.; Toney, M. F. Relationships between Lead Halide Perovskite Thin-Film Fabrication, Morphology, and Performance in Solar Cells. *J. Am. Chem. Soc.* **2016**, *138*, 463−470.

(23) Stranks, S. D.; Nayak, P. K.; Zhang, W.; Stergiopoulos, T.; Snaith, H. J. Formation of Thin Films of Organic-Inorganic Perovskites for High-Efficiency Solar Cells. *Angew. Chem., Int. Ed.* **2015**, *54*, 3240−3248.

(24) Zhao, Y.; Zhu, K. Solution Chemistry Engineering toward High-Efficiency Perovskite Solar Cells. *J. Phys. Chem. Lett.* **2014**, *5*, 4175−4186.

(25) Wang, Q.; Shao, Y.; Dong, Q.; Xiao, Z.; Yuan, Y.; Huang, J. Large Fill-Factor Bilayer Iodine Perovskite Solar Cells Fabricated by a Low-Temperature Solution-Process. *Energy Environ. Sci.* **2014**, *7*, 2359−2365.

(26) Williams, S. T.; Rajagopal, A.; Chueh, C.-C.; Jen, A. K.-Y. Current Challenges and Prospective Research for Upscaling Hybrid Perovskite Photovoltaics. *J. Phys. Chem. Lett.* **2016**, *7*, 811−819.

(27) Qiu, W.; Merckx, T.; Jaysankar, M.; Masse de la Huerta, C.; Rakocevic, L.; Zhang, W.; Paetzold, U. W.; Gehlhaar, R.; Froyen, L.; Poortmans, J.; et al. Pinhole-Free Perovskite Films for Efficient Solar Modules. *Energy Environ. Sci.* **2016**, *9*, 484−489.

(28) Ono, L. K.; Wang, S.; Kato, Y.; Raga, S. R.; Qi, Y. Fabrication of Semi-Transparent Perovskite Films with Centimeter-Scale Superior Uniformity by the Hybrid Deposition Method. *Energy Environ. Sci.* **2014**, *7*, 3989−3993.

(29) Leyden, M. R.; Lee, M. V.; Raga, S. R.; Qi, Y. Large Formamidinium Lead Trihalide Perovskite Solar Cells Using Chemical Vapor Deposition with High Reproducibility and Tunable Chlorine Concentrations. *J. Mater. Chem. A* **2015**, *3*, 16097−16103.

(30) Luo, P.; Liu, Z.; Xia, W.; Yuan, C.; Cheng, J.; Lu, Y. A Simple in Situ Tubular Chemical Vapor Deposition Processing of Large-Scale Efficient Perovskite Solar Cells and the Research on Their Novel Roll-over Phenomenon in J−V Curves. *J. Mater. Chem. A* **2015**, *3*, 12443−12451.

(31) Sutherland, B. R.; Hoogland, S.; Adachi, M. M.; Wong, C. T. O.; Sargent, E. H. Conformal Organohalide Perovskites Enable Lasing on Spherical Resonators. *ACS Nano* **2014**, *8*, 10947−10952.

(32) Chen, H.; Wei, Z.; Zheng, X.; Yang, S. A Scalable Electrodeposition Route to the Low-Cost, Versatile and Controllable Fabrication of Perovskite Solar Cells. *Nano Energy* **2015**, *15*, 216−226.

(33) Barrows, A.; Pearson, A.; Kwak, C.; Dunbar, A.; Buckley, A.; Lidzey, D. Efficient Planar Heterojunction Mixed-Halide Perovskite Solar Cells Deposited via Spray-Deposition. *Energy Environ. Sci.* **2014**, *7*, 2944−2950.

(34) Ramesh, M.; Boopathi, K. M.; Huang, T.-Y.; Huang, Y.-C.; Tsao, C.-S.; Chu, C.-W. Using an Airbrush Pen for Layer-by-Layer Growth of Continuous Perovskite Thin Films for Hybrid Solar Cells. *ACS Appl. Mater. Interfaces* **2015**, *7*, 2359−2366.

(35) Razza, S.; Di Giacomo, F.; Matteocci, F.; Cinà, L.; Palma, A. L.; Casaluci, S.; Cameron, P.; D'Epifanio, A.; Licoccia, S.; Reale, A.; et al.

DOI: 10.1021/acsomega.6b00351
ACS Omega 2016, 1, 1296−1306

Perovskite Solar Cells and Large Area Modules (100 cm^2) Based on an Air Flow-Assisted PbI_2 Blade Coating Deposition Process. *J. Power Sources* **2015**, *277*, 286−291.
(36) Back, H.; Kim, J.; Kim, G.; Kyun Kim, T.; Kang, H.; Kong, J.; Ho Lee, S.; Lee, K. Interfacial Modification of Hole Transport Layers for Efficient Large-Area Perovskite Solar Cells Achieved via Blade-Coating. *Sol. Energy Mater. Sol. Cells* **2016**, *144*, 309−315.
(37) Therese, G. H. A.; Kamath, P. V. Electrochemical Synthesis of Metal Oxides and Hydroxides. *Chem. Mater.* **2000**, *12*, 1195−1204.
(38) Rajeshwar, K. Electrosynthesized Thin Films of Group II−VI Compound Semiconductors, Alloys and Superstructures. *Adv. Mater.* **1992**, *4*, 23−29.
(39) Chen, Q.; Zhou, H.; Hong, Z.; Luo, S.; Duan, H.; Wang, H.; Liu, Y.; Li, G.; Yang, Y. Planar Heterojunction Perovskite Solar Cells via Vapor-Assisted Solution Process. *J. Am. Chem. Soc.* **2014**, *136*, 622−625.
(40) Tosun, B. S.; Hillhouse, H. W. Enhanced Carrier Lifetimes of Pure Iodide Hybrid Perovskite via Vapor-Equilibrated Re-Growth (VERG). *J. Phys. Chem. Lett.* **2015**, *6*, 2503−2508.
(41) Seol, D.-J.; Lee, J.-W.; Park, N.-G. On the Role of Interfaces in Planar-Structured $HC(NH_2)_2PbI_3$ Perovskite Solar Cells. *ChemSusChem* **2015**, *8*, 2414−2419.
(42) Liang, K.; Mitzi, D. B.; Prikas, M. T. Synthesis and Characterization of Organic−Inorganic Perovskite Thin Films Prepared Using a Versatile Two-Step Dipping Technique. *Chem. Mater.* **1998**, *10*, 403−411.
(43) Tan, Y. J.; Lim, K. Y. Understanding and Improving the Uniformity of Electrodeposition. *Surf. Coat. Technol.* **2003**, *167*, 255−262.
(44) Mindt, W. Electrical Properties of Electrodeposited PbO_2 Films. *J. Electrochem. Soc.* **1969**, *116*, 1076−1080.
(45) Scanlon, D. O.; Kehoe, A. B.; Watson, G. W.; Jones, M. O.; David, W. I. F.; Payne, D. J.; Egdell, R. G.; Edwards, P. P.; Walsh, A. Nature of the Band Gap and Origin of the Conductivity of PbO_2 Revealed by Theory and Experiment. *Phys. Rev. Lett.* **2011**, *107*, No. 246402.
(46) Cui, X.-P.; Jiang, K.-J.; Huang, J.-H.; Zhou, X.-Q.; Su, M.-J.; Li, S.-G.; Zhang, Q.-Q.; Yang, L.-M.; Song, Y.-L. Electrodeposition of PbO and In Situ Conversion to $CH_3NH_3PbI_3$ for Mesoscopic Perovskite Solar Cells. *Chem. Commun.* **2015**, *51*, 1457−1460.
(47) Huang, J.-H.; Jiang, K.-J.; Cui, X.-P.; Zhang, Q.-Q.; Gao, M.; Su, M.-J.; Yang, L.-M.; Song, Y. Direct Conversion of $CH_3NH_3PbI_3$ from Electrodeposited PbO for Highly Efficient Planar Perovskite Solar Cells. *Sci. Rep.* **2015**, *5*, No. 15889.
(48) Ferreira da Silva, A.; Veissid, N.; An, C. Y.; Pepe, I.; Barros de Oliveira, N.; Batista da Silva, A. V. Optical Determination of the Direct Bandgap Energy of Lead Iodide Crystals. *Appl. Phys. Lett.* **1996**, *69*, 1930−1932.
(49) Brenner, T. M.; Rakita, Y.; Orr, Y.; Klein, E.; Feldman, I.; Elbaum, M.; Cahen, D.; Hodes, G. Conversion of Single Crystalline PbI_2 to $CH_3NH_3PbI_3$: Structural Relations and Transformation Dynamics. *Chem. Mater.* **2016**, *28*, 6501−6510.
(50) Stoumpos, C. C.; Malliakas, C. D.; Kanatzidis, M. G. Semiconducting Tin and Lead Iodide Perovskites with Organic Cations: Phase Transitions, High Mobilities, and Near-Infrared Photoluminescent Properties. *Inorg. Chem.* **2013**, *52*, 9019−9038.
(51) Milot, R. L.; Eperon, G. E.; Snaith, H. J.; Johnston, M. B.; Herz, L. M. Temperature-Dependent Charge-Carrier Dynamics in $CH_3NH_3PbI_3$ Perovskite Thin Films. *Adv. Funct. Mater.* **2015**, *25*, 6218−6227.
(52) Cojocaru, L.; Uchida, S.; Sanehira, Y.; Gonzalez-Pedro, V.; Bisquert, J.; Nakazaki, J.; Kubo, T.; Segawa, H. Temperature Effects on the Photovoltaic Performance of Planar Structure Perovskite Solar Cells. *Chem. Lett.* **2015**, *44*, 1557−1559.
(53) Xiao, Z.; Dong, Q.; Bi, C.; Shao, Y.; Yuan, Y.; Huang, J. Solvent Annealing of Perovskite-Induced Crystal Growth for Photovoltaic-Device Efficiency Enhancement. *Adv. Mater.* **2014**, *26*, 6503−6509.
(54) Raga, S. R.; Jung, M.-C.; Lee, M. V.; Leyden, M. R.; Kato, Y.; Qi, Y. Influence of Air Annealing on High Efficiency Planar Structure Perovskite Solar Cells. *Chem. Mater.* **2015**, *27*, 1597−1603.
(55) Dong, Q.; Yuan, Y.; Shao, Y.; Fang, Y.; Wang, Q.; Huang, J. Abnormal Crystal Growth in $CH_3NH_3PbI_{3-x}Cl_x$ Using a Multi-Cycle Solution Coating Process. *Energy Environ. Sci.* **2015**, *8*, 2464−2470.
(56) Leguy, A. M. A.; Hu, Y.; Campoy-Quiles, M.; Alonso, M. I.; Weber, O. J.; Azarhoosh, P.; van Schilfgaarde, M.; Weller, M. T.; Bein, T.; Nelson, J.; et al. Reversible Hydration of $CH_3NH_3PbI_3$ in Films, Single Crystals, and Solar Cells. *Chem. Mater.* **2015**, *27*, 3397−3407.
(57) Manser, J. S.; Saidaminov, M. I.; Christians, J. A.; Bakr, O. M.; Kamat, P. V. Making and Breaking of Lead Halide Perovskites. *Acc. Chem. Res.* **2016**, *49*, 330−338.
(58) Bartlett, P. N.; Dunford, T.; Ghanem, M. A. Templated Electrochemical Deposition of Nanostructured Macroporous PbO_2. *J. Mater. Chem.* **2002**, *12*, 3130−3135.
(59) Waldo, R. A. An Iteration Procedure to Calculate Film Compositions and Thicknesses in Electron-Probe Microanalysis. *Microbeam Analysis*; Newbury, D. E., Ed.; San Francisco Press: San Francisco, 1988; 310−314.
(60) Nečas, D.; Klapetek, P. Gwyddion: An Open-Source Software for SPM Data Analysis. *Open Phys.* **2011**, *10*, 181−188.
(61) Swanepoel, R. Determination of the Thickness and Optical Constants of Amorphous Silicon. *J. Phys. E: Sci. Instrum.* **1983**, *16*, 1214−1222.
(62) Sreemany, M.; Sen, S. A Simple Spectrophotometric Method for Determination of the Optical Constants and Band Gap Energy of Multiple Layer TiO_2 Thin Films. *Mater. Chem. Phys.* **2004**, *83*, 169−177.

DOI: 10.1021/acsomega.6b00351
ACS Omega 2016, 1, 1296−1306